The structural origin of second harmonic generation in fascia

Maxime Rivard,[1] Mathieu Laliberté,[1] Antony Bertrand-Grenier,[1] Catalin Harnagea,[1] Christian P. Pfeffer,[2] Martin Vallières,[1] Yves St-Pierre,[3] Alain Pignolet,[1] My Ali El Khakani,[1] and François Légaré[1,*]

[1]*Institut National de la Recherche Scientifique, Centre Énergie Matériaux et Télécommunications, 1650 Boulevard Lionel-Boulet, Varennes, Qc Canada J3X1S2*
[2] *Harvard School of Dental Medicine, 188 Longwood Avenue, Boston, MA 02115, USA*
[3] *Institut National de la Recherche Scientifique, Institut Armand-Frappier, 531 boul. des Prairies, Laval, Qc Canada H7V 1B7*
*legare@emt.inrs.ca

Abstract: Fascia tissue is rich in collagen type I proteins and can be imaged by second harmonic generation (SHG) microscopy. While identifying the overall alignment of the collagen fibrils is evident from those images, the tridimensional structural origin for the observation of SHG signal is more complex than it apparently seems. Those images reveal that the noncentrosymmetric (piezoelectric) structures are distributed heterogeneously on spatial dimensions inferior to the resolution provided by the nonlinear optical microscope (sub-micron). Using piezoresponse force microscopy (PFM), we show that an individual collagen fibril has a noncentrosymmetric structural organization. Fibrils are found to be arranged in nano-domains where the anisotropic axis is preserved along the fibrillar axis, while across the collagen sheets, the phase of the second order nonlinear susceptibility is changing by 180 degrees between adjacent nano-domains. This complex architecture of noncentrosymmetric nano-domains governs the coherent addition of 2ω light within the focal volume and the observed features in the SHG images taken in fascia.

References and links

1. P. J. Campagnola, A. C. Millard, M. Terasaki, P. E. Hoppe, C. J. Malone, and W. A. Mohler, "Three-dimensional high-resolution second-harmonic generation imaging of endogenous structural proteins in biological tissues," Biophys. J. **82**(1), 493–508 (2002).
2. E. Brown, T. McKee, E. diTomaso, A. Pluen, B. Seed, Y. Boucher, and R. K. Jain, "Dynamic imaging of collagen and its modulation in tumors in vivo using second-harmonic generation," Nat. Med. **9**(6), 796–801 (2003).
3. P. Stoller, P. M. Celliers, K. M. Reiser, and A. M. Rubenchik, "Quantitative second-harmonic generation microscopy in collagen," Appl. Opt. **42**(25), 5209–5219 (2003).
4. R. M. Williams, W. R. Zipfel, and W. W. Webb, "Interpreting second-harmonic generation images of collagen I fibrils," Biophys. J. **88**(2), 1377–1386 (2005).
5. A. T. Yeh, M. J. Hammer-Wilson, D. C. Van Sickle, H. P. Benton, A. Zoumi, B. J. Tromberg, and G. M. Peavy, "Nonlinear optical microscopy of articular cartilage," Osteoarthritis Cartilage **13**(4), 345–352 (2005).
6. J. C. Mansfield, C. P. Winlove, J. Moger, and S. J. Matcher, "Collagen fiber arrangement in normal and diseased cartilage studied by polarization sensitive nonlinear microscopy," J. Biomed. Opt. **13**(4), 044020 (2008).
7. S. V. Plotnikov, A. C. Millard, P. J. Campagnola, and W. A. Mohler, "Characterization of the myosin-based source for second-harmonic generation from muscle sarcomeres," Biophys. J. **90**(2), 693–703 (2006).
8. S.-W. Chu, S.-Y. Chen, G.-W. Chern, T. H. Tsai, Y. C. Chen, B.-L. Lin, and C.-K. Sun, "Studies of $\chi^{(2)}/\chi^{(3)}$ tensors in submicron-scaled bio-tissues by polarization harmonics optical microscopy," Biophys. J. **86**(6), 3914–3922 (2004).
9. T. Boulesteix, E. Beaurepaire, M.-P. Sauviat, and M.-C. Schanne-Klein, "Second-harmonic microscopy of unstained living cardiac myocytes: measurements of sarcomere length with 20-nm accuracy," Opt. Lett. **29**(17), 2031–2033 (2004).
10. W. H. Stoothoff, B. J. Bacskai, and B. T. Hyman, "Monitoring tau-tubulin interactions utilizing second harmonic generation in living neurons," J. Biomed. Opt. **13**(6), 064039 (2008).

11. A. Zoumi, A. Yeh, and B. J. Tromberg, "Imaging cells and extracellular matrix in vivo by using second-harmonic generation and two-photon excited fluorescence," Proc. Natl. Acad. Sci. U.S.A. **99**(17), 11014–11019 (2002).
12. W. R. Zipfel, R. M. Williams, R. Christie, A. Y. Nikitin, B. T. Hyman, and W. W. Webb, "Live tissue intrinsic emission microscopy using multiphoton-excited native fluorescence and second harmonic generation," Proc. Natl. Acad. Sci. U.S.A. **100**(12), 7075–7080 (2003).
13. D. Oron, D. Yelin, E. Tal, S. Raz, R. Fachima, and Y. Silberberg, "Depth-resolved structural imaging by third-harmonic generation microscopy," J. Struct. Biol. **147**(1), 3–11 (2004).
14. D. Débarre, W. Supatto, A. M. Pena, A. Fabre, T. Tordjmann, L. Combettes, M. C. Schanne-Klein, and E. Beaurepaire, "Imaging lipid bodies in cells and tissues using third-harmonic generation microscopy," Nat. Methods **3**(1), 47–53 (2006).
15. H. Wang, Y. Fu, P. Zickmund, R. Shi, and J. X. Cheng, "Coherent anti-stokes Raman scattering imaging of axonal myelin in live spinal tissues," Biophys. J. **89**(1), 581–591 (2005).
16. C. L. Evans, E. O. Potma, M. Puoris'haag, D. Côté, C. P. Lin, and X. S. Xie, "Chemical imaging of tissue in vivo with video-rate coherent anti-Stokes Raman scattering microscopy," Proc. Natl. Acad. Sci. U.S.A. **102**(46), 16807–16812 (2005).
17. A. F. Pegoraro, A. D. Slepkov, A. Ridsdale, J. P. Pezacki, and A. Stolow, "Single laser source for multimodal coherent anti-Stokes Raman scattering microscopy," Appl. Opt. **49**(25), F10–F17 (2010).
18. C. W. Freudiger, W. Min, B. G. Saar, S. Lu, G. R. Holtom, C. He, J. C. Tsai, J. X. Kang, and X. S. Xie, "Label-free biomedical imaging with high sensitivity by stimulated Raman scattering microscopy," Science **322**(5909), 1857–1861 (2008).
19. P. Nandakumar, A. Kovalev, and A. Volkmer, "Vibrational imaging based on stimulated Raman scattering microscopy," N. J. Phys. **11**(3), 033026 (2009).
20. A. Volkmer, J.-X. Cheng, and X. Sunney Xie, "Vibrational imaging with high sensitivity via epidetected coherent anti-Stokes Raman scattering microscopy," Phys. Rev. Lett. **87**(2), 023901 (2001).
21. T. A. Theodossiou, C. Thrasivoulou, C. Ekwobi, and D. L. Becker, "Second harmonic generation confocal microscopy of collagen type I from rat tendon cryosections," Biophys. J. **91**(12), 4665–4677 (2006).
22. O. Nadiarnykh, R. B. Lacomb, P. J. Campagnola, and W. A. Mohler, "Coherent and incoherent SHG in fibrillar cellulose matrices," Opt. Express **15**(6), 3348–3360 (2007).
23. F. Légaré, C. P. Pfeffer, and B. R. Olsen, "The role of backscattering in SHG tissue imaging," Biophys. J. **93**(4), 1312–1320 (2007).
24. P. Bianchini, and A. Diaspro, "Three-dimensional (3D) backward and forward second harmonic generation (SHG) microscopy of biological tissues," J Biophotonics **1**(6), 443–450 (2008).
25. R. Lacomb, O. Nadiarnykh, S. S. Townsend, and P. J. Campagnola, "Phase matching considerations in second harmonic generation from tissues: Effects on emission directionality, conversion efficiency and observed morphology," Opt. Commun. **281**(7), 1823–1832 (2008).
26. S.-W. Chu, S.-P. Tai, T.-M. Liu, C.-K. Sun, and C. H. Lin, "Selective imaging in second-harmonic-generation microscopy with anisotropic radiation," J. Biomed. Opt. **14**(1), 010504 (2009).
27. R. A. Rao, M. R. Mehta, S. Leithem, and K. C. Toussaint, Jr., "Quantitative analysis of forward and backward second-harmonic images of collagen fibers using Fourier transform second-harmonic-generation microscopy," Opt. Lett. **34**(24), 3779–3781 (2009).
28. J. Mertz, and L. Moreaux, "Second-harmonic generation by focused excitation of inhomogeneously distributed scatterers," Opt. Commun. **196**(1-6), 325–330 (2001).
29. K. Kühn, "The structure of collagen," Essays Biochem. **5**, 59–87 (1969).
30. K. E. Kadler, A. Hill, and E. G. Canty-Laird, "Collagen fibrillogenesis: fibronectin, integrins, and minor collagens as organizers and nucleators," Curr. Opin. Cell Biol. **20**(5), 495–501 (2008).
31. K. E. Kadler, D. F. Holmes, J. A. Trotter, and J. A. Chapman, "Collagen fibril formation," Biochem. J. **316**(Pt 1), 1–11 (1996).
32. D. R. Baselt, J. P. Revel, and J. D. Baldeschwieler, "Subfibrillar structure of type I collagen observed by atomic force microscopy," Biophys. J. **65**(6), 2644–2655 (1993).
33. M. F. Paige, J. K. Rainey, and M. C. Goh, "Fibrous long spacing collagen ultrastructure elucidated by atomic force microscopy," Biophys. J. **74**(6), 3211–3216 (1998).
34. D. F. Holmes, M. P. Lowe, and J. A. Chapman, "Vertebrate (chick) collagen fibrils formed *in vivo* can exhibit a reversal in molecular polarity," J. Mol. Biol. **235**(1), 80–83 (1994).
35. J. Hulliger, "Connective tissue polarity unraveled by a Markov-chain mechanism of collagen fibril segment self-assembly," Biophys. J. **84**(6), 3501–3507 (2003).
36. I. Rocha-Mendoza, D. R. Yankelevich, M. Wang, K. M. Reiser, C. W. Frank, and A. Knoesen, "Sum frequency vibrational spectroscopy: the molecular origins of the optical second-order nonlinearity of collagen," Biophys. J. **93**(12), 4433–4444 (2007).
37. M. Strupler, and M.-C. Schanne-Klein, "Simulating second harmonic generation from tendon - Do we see fibrils?" in *Biomedical Optics*, OSA Technical Digest (CD) (Optical Society of America, 2010), paper BTuD83.
38. D. A. D. Parry, and A. S. Craig, "Quantitative electron microscope observations of the collagen fibrils in rat-tail tendon," Biopolymers **16**(5), 1015–1031 (1977).
39. C. Harnagea, A. Pignolet, M. Alexe, and D. Hesse, "Higher-order electromechanical response of thin films by contact resonance piezoresponse force microscopy," IEEE Trans. Ultrason. Ferroelectr. Freq. Control **53**(12), 2309–2322 (2006).
40. B. P. Chan, C. Amann, A. N. Yaroslavsky, C. Title, D. Smink, B. Zarins, I. E. Kochevar, and R. W. Redmond, "Photochemical repair of Achilles tendon rupture in a rat model," J. Surg. Res. **124**(2), 274–279 (2005).

41. C. Harnagea, M. Vallières, C. P. Pfeffer, D. Wu, B. R. Olsen, A. Pignolet, F. Légaré, and A. Gruverman, "Two-dimensional nanoscale structural and functional imaging in individual collagen type I fibrils," Biophys. J. **98**(12), 3070–3077 (2010).
42. M. Minary-Jolandan, and M.-F. Yu, "Uncovering Nanoscale Electromechanical Heterogeneity in the Subfibrillar Structure of Collagen Fibrils Responsible for the Piezoelectricity of Bone," ACS Nano **3**(7), 1859–1863 (2009).
43. A. Kholkin, N. Amdursky, I. Bdikin, E. Gazit, and G. Rosenman, "Strong piezoelectricity in bioinspired peptide nanotubes," ACS Nano **4**(2), 610–614 (2010).

1. Introduction

Second harmonic generation (SHG) microscopy is a powerful technique for high spatial resolution label free imaging of biological structures possessing a noncentrosymmetric (piezoelectric) structural organization such as connective tissues rich in collagen type I-III proteins [1–4], cartilage rich in collagen type II [5,6], the myosin band within the sarcomere of skeletal and cardiac muscle [7–9], and the microtubules [2,10]. This technique is commonly used simultaneously with two photon fluorescence microscopy because both are using the same experimental setup, namely a laser scanning microscope and a femtosecond laser source [11,12]. The SHG signal is easily distinguished and isolated from the fluorescence since it is exactly centered at twice the frequency of the excitation laser source.

As opposed to two photon fluorescence microscopy, SHG microscopy is based on a coherent nonlinear optical process of second order that does not require electronic excitation. This is a major advantage compared to fluorescence as electronic excitation results in phototoxicity and photobleaching. Third harmonic generation (THG) [13,14], coherent anti-Stokes Raman scattering (CARS) [15–17], and stimulated Raman scattering [18,19] also benefit from these two advantages over fluorescence. The coherent nature of the SHG, THG and CARS processes makes it more complicated to interpret the obtained images than with fluorescence imaging contrast. Indeed, the strength of the generated signal depends on the detection direction relative to the laser propagation and the signal in the forward direction reveals different structural information than in the backward direction [4,20–27]. In consequence, the signal not only depends on the density of scatterers but also on the overall structural organization within the focal volume of the microscope objective. This has been nicely illustrated for SHG microscopy by modeling the signal and the radiation pattern from an inhomogeneously distribution of $\chi^{(2)}$ scatterers [28].

Collagen type I is the most abundant structural protein in higher vertebrates and is the building block of highly organized tissue structures [29,30]. Collagen type I fibrils are constructed from a highly regular assembly of tropocollagen molecules (280 nm long, 1.5nm in diameter), which are formed as the procollagens (made of three preprocollagen molecules) enter the extracellular environment. They spontaneously self-assemble into a regularly staggered array with a characteristic 67 nm banding pattern [31–33]. Fibrils are polar structures, which means that they are noncentrosymmetric and piezoelectric, and an axial alignment of domains with anti-parallel polarity along the fibrillar axis has been reported [34]. At the macroscopic scale, the partial polar order observed in collageneous tissues has been modeled using a Markov-chain mechanism [35] and explains the observation of SHG. Recently, the molecular origin of SHG has been elucidated using sum-frequency generation vibrational spectroscopy [36].

Despite those extensive studies, the structural organization of the $\chi^{(2)}$ scatterers at the sub-micron spatial scale remains a matter of debate. The forward to backward signal ratio and the differences in the SHG images acquired in the two directions have been discussed in several publications [4,21–27]. The experimental observations are directly linked to the structural arrangement of the $\chi^{(2)}$ scatterers within the focal volume but the spatial resolution provided by SHG microscopy is not sufficient to elucidate this complex organization of noncentrosymmetric structures at the nanoscale. Two hypotheses have been elaborated to interpret SHG from tissues rich in collagen type I proteins: (1) Williams et *al.* have modeled the nonlinear optical interaction assuming that the collagen fibrils are cylinders with the $\chi^{(2)}$ scatterers distributed uniformly at the surface of the cylinders [4]; (2) Strupler and Schanne-Klein have also assumed a cylindrical shape for the fibrils (with $\chi^{(2)}$ scatterers distributed

either uniformly within their volume or only at their surface) but, additionally, they allowed the phase of $\chi^{(2)}$ to flip by 180 degrees from one fibril to another [37]. This idea of a complex structural organization of $\chi^{(2)}$ scatterers distributed among domains was discussed by LaComb et al. [25]. This second hypothesis is supported by electron microscopy measurements on rat tail tendons [38].

In this paper, we report imaging of thin sections (~10 μm of thickness) of *ex-vivo* fascia tissue with SHG and Piezoresponse Force Microscopy (PFM) techniques to confirm which one of the two hypotheses explains the SHG microscopy measurements. Forward and backward SHG images have been acquired simultaneously in fascia and suggest that the distribution of $\chi^{(2)}$ scatterers is heterogeneous on a spatial scale inferior to the resolution provided by the nonlinear optical microscope (sub-micron). In addition, by varying the aperture diameter in the forward direction, new features in the forward SHG images are observed showing that the radiation pattern is changing as the laser is scanned across the collagen array. Since experiments in crystalline quartz demonstrate that the SHG radiation pattern depends on the distribution of $\chi^{(2)}$ scatterers within the focal volume, the variation of the SHG radiation pattern while scanning the tissue is furthermore illustrating a complex arrangement of $\chi^{(2)}$ scatterers at the sub-micron level. Since the structural requirement for the observation of SHG is the same as for the existence of piezoelectricity, i.e. noncentrosymmetricity, we used PFM to image the piezoelectric properties of fascia. This scanning probe technique provides sub-10 nanometers resolution and allows mapping the spatial distribution of noncentrosymmetric structures within the collagen sheets of fascia down to the dimension of an individual collagen fibril.

2. Experimental section

2.1 SHG experiments

A laser scanning optical microscope was used to perform the experiments; (1) SHG imaging of thin section (~10 μm of thickness) of ex vivo fascia, and (2) SHG from a 350 microns thick quartz slab. The experimental layout is presented in Fig. 1. The laser source was a ~150 fs pulse duration Titanium-Sapphire oscillator with a repetition rate of 80 MHz (Tsunami, Spectra Physics, Santa Clara, USA). The central wavelength was tuned at 810 nm. After the oscillator, the average power was controlled using the combination of a half-wave plate and a polarizer. Subsequently to the energy attenuator, the spatial profile of the laser beam was cleaned by focusing through a pinhole with a diameter of 50 microns.
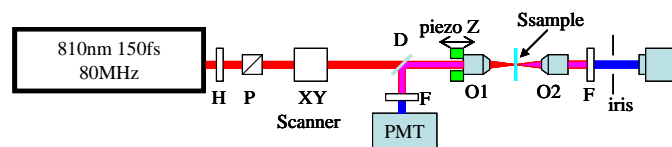

Fig. 1. Experimental setup used for the SHG experiments: forward and backward SHG imaging microscopy, forward SHG microscopy with a variable collection numerical aperture (iris) and SHG under tight focusing near a quartz interface (radiation pattern measurement). H, half-wave plate; P, polarizer; D, Dichroic mirror; O1, illumination objective (0.8 NA, water); O2, collection objective (1.15 NA, water); F, filters; PMT, photomultiplier tube. In the forward direction, the detector is whether a PMT or a CCD.

For the SHG experiments, we used a laser scanning inverted microscope (Till Photonics GmbH, Munich, Germany). The focusing objective used in our experiments was the Olympus LUMPLFLN 40XW (water immersion with a numerical aperture of 0.8). The size of the laser beam at the entrance of the XY scanner was set to ensure that the aperture of the focusing objective was completely illuminated. Its position relative to the sample was controlled by a mechanic and a piezoelectric motor for coarse and fine adjustment. In the forward direction, SHG light is collected with another microscope objective, the Olympus UAPO 40XW3/340 (water immersion with a numerical aperture of 1.15). By using a collection objective with a numerical aperture higher than the focusing one, efficient detection of the forward SHG light

is ensured. The XYZ position of the collection objective was carefully adjusted with a micrometric positioner to ensure a collimated beam propagating along the same path as it would if the two objectives were absent. Along that light path in the forward direction, a centered graduated iris was installed such that the effective collection numerical aperture can be controlled. In both direction of detection (forward and backward), photomultiplier tubes (PMT) were installed to detect the SHG light from which 810 nm was filtered out with narrow bandpass filters (405 ± 5nm). In the forward direction, for the experiments with the quartz slab, a CCD camera was also installed to analyze angular distribution of the SHG intensity (also called the radiation pattern).

2.2 PFM experiments

To image noncentrosymmetric nano-domains with lateral resolution below 10 nm, we used atomic force microscopy in piezoresponse mode (Piezoresponse Force Microscopy, PFM). In this mode, a conductive tip brought in contact with the surface of the sample is used as a movable electrode. A periodic electric field is created locally in the sample by applying an AC bias voltage between the tip and a conductive electrode on which the sample is prepared. The electric field induces a sample surface synchronous vibration - representing the local piezoelectric response which is transmitted to the cantilever via the same tip. The cantilever vibration is extracted from the global deflection using a lock-in detection scheme. While this scanning probe technique allows the detection of both out-of plane and in-plane sample surface displacements, in the experiments presented here, we detected only in-plane displacements. The local piezoelectric measurements were carried out using a setup described in detail earlier [39]. The Atomic Force Microscope (Enviroscope, Veeco Instruments) equipped with soft CSC38 (Mikromasch) cantilevers (k = 0.07 N/m) coated with Cr/Au was operated in contact mode, with a typical contact force of 2 nN. A small AC voltage (0.5 V, 29 kHz) was applied between the conductive tip and the platinum coated substrate. We then detected the cantilever vibrations induced by the surface displacements in the contact region using two lock-in amplifiers from Signal Recovery (model 7265).

2.3 Sample preparation

Fascia tissue was harvested *in situ*, under a Nikon dissecting microscope from the anterior tibialis muscle of C57BL/6 mice after euthanasia. The fascia tissue was fixed for 1-2h in 4% PFA at 4°C (4% w/v solution of paraformaldehyde (PFA) diluted in PBS). A 3mm × 3mm fascia piece was then transferred to either glass plates (for SHG experiments) or to electrically conductive substrates (platinized silicon wafers, for performing PFM). For optimal adhesion of the tissue, the substrates were treated with a gelatin-chromium potassium sulfate solution (Gelatin type A- Sigma®, Chromium potassium sulphate, Sigma) before tissue deposition transfer. The thickness of the fascia tissue is about 10 μm.

3. Results and discussion

3.1 Forward vs backward SHG imaging of fascia

The first experiment on thin slice of fascia tissue consists in comparing the SHG images acquired in the forward and the backward direction. The laser beam is focussed at a plane that is scanned in a thin slice of fascia tissue placed on a 150 μm thick microscope slide mounted on a XY translation platform to image different areas of the tissue. By using a slice of tissue with ~10 microns of thickness, we ensure that the contribution of backscattered forward SHG light is negligible. Such thickness is much smaller than the characteristic mean free path for light scattering in collagen type-I rich tissue [40]. Additionally, backward SHG images are collected while removing the forward detection condenser to avoid the contribution of forward SHG light due to Fresnel reflection at optical interfaces.

   The SHG signal measured in the backward direction is in average ~5 times weaker than the measured signal in the forward direction. A weaker signal is expected because of poorer phase matching condition in the backward direction. However, the backward SHG signal in

fascia is large compared to the backward SHG signal obtained from bulk media since it vanishes for an homogeneous distribution of $\chi^{(2)}$ scatterers within the focal volume [28]. This small ratio between forward and backward signal suggests that the distribution of noncentrosymmetric structures in fascia is heterogeneous within the focal volume.

Figure 2(a,b) represents typical forward and backward images. When the laser polarization is along the X axis, the SHG signal in both direction of detection is the largest defining the fibrillar axis of fascia and in general of any tissue rich in collagen type-I proteins [4]. In this paper, we only present results obtained in this experimental configuration since we have not seen any dependence on the FWD/BWD signal ratio while changing the laser polarization (the images remain identical under signal normalization). In the forward images (blue curves), one can observe that the SHG signal is quite smooth along the longitudinal direction – X axis (Fig. 2(c)) – while it is highly modulated transverse – Y axis – to the fibrillar axis with sharp peaks and large amplitude modulations (Fig. 2(d)). Transverse to the fibrillar axis, one can observe clear boundaries defining the collagen sheets of fascia only in the backward direction. At those boundaries, the SHG signal is zero in both direction of detection indicating the absence of noncentrosymmetric structures. Boundaries are indicated in Fig. 2(d).
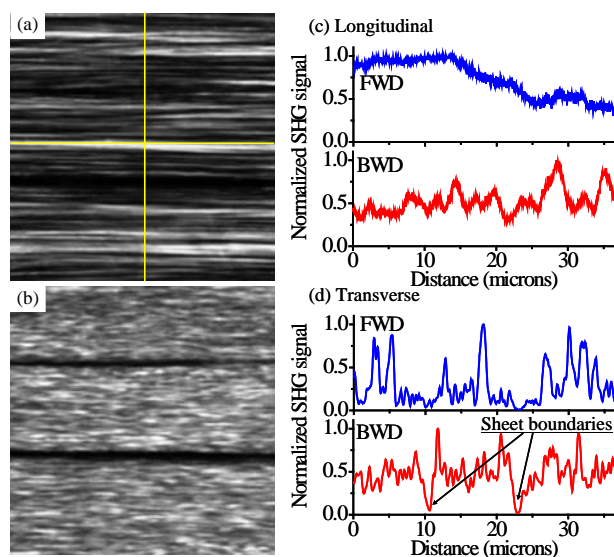

Fig. 2. SHG images of fascia tissue in (a) forward and (b) backward direction. Signal profiles taken along the same lines in forward and backward images (c) longitudinally and (d) transverse to the collagen sheets. Longitudinal and transverse (to the fibrillar axis) intensity profiles were taken along the yellow lines. The boundaries between the collagen sheets are clear in the backward direction.

Across the collagen sheets, the backward SHG signal never vanished indicating the presence of noncentrosymmetric structures everywhere within the spatial resolution provided by the nonlinear optical microscope which is sub-micron in the XY plane. In backward, there are no sharp peaks with large modulations as observed in the transverse direction of the forward images. This reveals that the smooth features observed in the forward images are not individual collagen fibers. A plausible explanation for the signal distribution in the forward image would be that $\chi^{(2)}$ domains boundaries are encountered transversally (and possibly in the direction of light propagation), but not longitudinally. Therefore, as the laser beam is scanned transversely, the phase-matching condition is changing rapidly and the forward signal gets highly modulated. This would explain the presence of dark lines within the collagen sheets of forward images which can be falsely interpreted as the absence of collagen fibrils. In summary, it appears that bundles of fibrils form $\chi^{(2)}$ domains in the tissue where phase matching condition is better satisfied in the forward direction. To further explore this

hypothesis, we looked at the SHG radiation pattern of the tissue since it should change in a material containing different $\chi^{(2)}$ domains within spatial dimension of the focal volume.

3.2 Forward SHG imaging of fascia as a function of the collection numerical aperture

By modeling SHG of an heterogeneous distribution of $\chi^{(2)}$ scatterers located on the axis of laser propagation, Mertz et *al.* have shown that the FWD/BWD signal ratio correlates with the shape of the radiation pattern [28]. To investigate the SHG radiation pattern from fascia tissue, images were taken while varying the effective collection numerical aperture (NA). Our CCD camera is not sensitive enough to detect the SHG radiation pattern. The images presented in Fig. 3 were acquired at different laser powers (in the 25 to 100 mW range) at the focus in order to compensate for the decrease of signal while reducing the numerical aperture (NA) of collection.
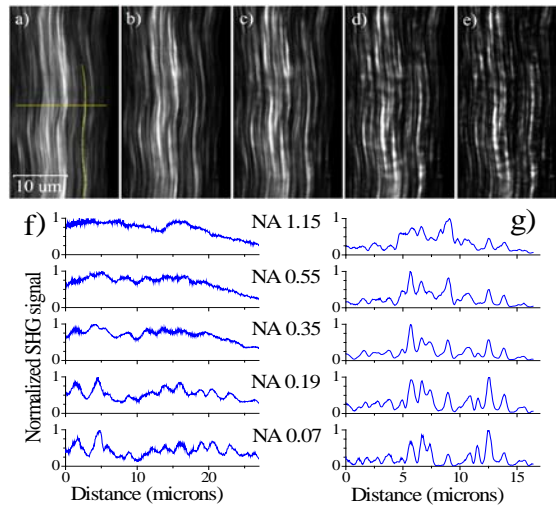

Fig. 3. SHG images of fascia tissue taken with different collection NA by varying the aperture of the collection objective with an iris. Forward signal was collected with (a) 1,15 NA, (b) 0,55 NA, (c) 0,35 NA, (d) 0,19 NA and (e) 0,07 NA. Longitudinal and transversal (to the fibrillar axis) intensity profiles taken in (a-e) along the yellow lines shown in (a) are also presented in (f) and (g). New modulations in the signal appear along those structures when the collection NA used to take the image is smaller than 0.55.

The images taken with different collection NA are similar to each others. However, new modulations appear in the image when the collection NA is reduced. This means that the angle of emission of the SHG is not the same everywhere in the image otherwise no changes other than a drop in the signal would be observed when reducing the collection NA. The modulations are very clear when using a very small collection NA, but they are still apparent even at higher collection NA. The presence of those modulations due to changes in the radiation pattern are another clear indication that the distribution of $\chi^{(2)}$ scatterers within fascia is heterogeneous at the sub-micron scale. In particular, one can observe in the transversal profiles (Fig. 3(g)) that new peaks are becoming predominant while changing the collection NA. Despite the fact that varying the collection objective's effective NA with an iris might look like a rudimentary setup, the next experiment demonstrates its validity for detecting changes in the distribution of noncentrosymmetric structures within the focal volume.

3.3 Forward SHG radiation pattern from crystalline quartz

SHG from crystalline quartz was characterized to serve as a model for better understanding the effect of closing the iris while measuring the 2ω signal. This model experiment consisted in taking SHG signal profiles in Z (axis of optical propagation) near the upper and lower air-

quartz interfaces and at different effective collection NA by closing the iris installed in the forward direction.
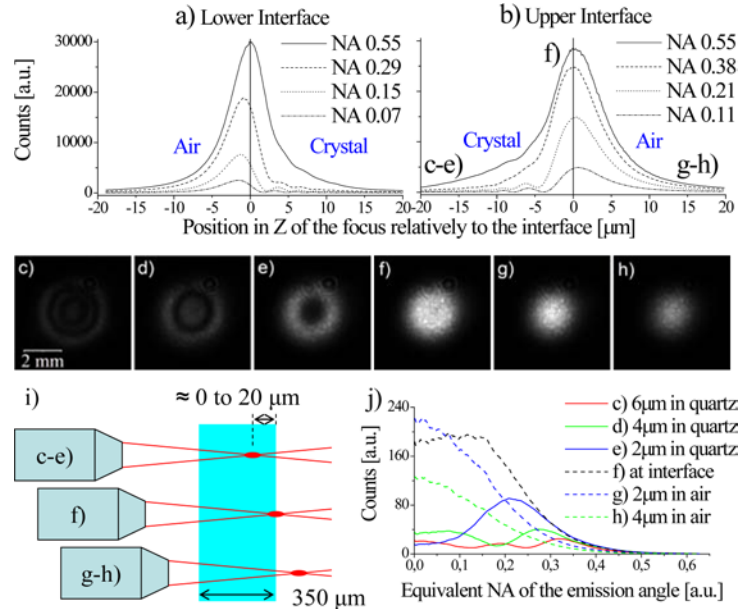

Fig. 4. Experimental signal profiles when (i) the focus travels through (a) the lower and (b) the upper interface of the quartz crystal. When the NA used for collection is reduced, the SHG signal profile becomes asymmetric in Z at both interfaces. Images of the collimated radiation pattern are taken with a CCD camera while the focus is near the upper interface: (c) 6 μm in the crystal, (d) 4 μm in the crystal, (e) 2 μm in the crystal, (f) at the interface, (g) 2 μm in the air and (h) 4 μm in the air. (j) The radial intensity profile in function of the equivalent NA (which is a measure of the angle of emission). This demonstrates that the position of the focus in the $\chi^{(2)}$ distribution can be responsible for changes in the radiation pattern.

The beam is focused near the upper or lower interface of a quartz crystal slab mounted on a Z translation stage with a precision better than 1 μm. The experiment is described in Fig. 4(i) for the upper interface. After collimating the SHG beam with the collection objective, both objectives remain immobile for the rest of the experiment to maintain the collimation. The distance between the focus and the quartz crystal interfaces is adjusted with the Z translation stage. The quartz crystal slab is 350 μm thick and is double-side polished. Its Y optical axis is normal to its polished surface and parallel to the laser propagation. Its X and Z optical axis are in the plane of the thin crystal and the laser polarization is aligned with the quartz' X optical axis to maximize SHG from the d_{11} element (contracted notation) of the $\chi^{(2)}$ tensor. Both objectives have enough working distance to reach the lower or upper interface of the quartz crystal slab.

The SHG signal profiles obtained for different NA of collection are presented in Figs. 4(a), 4(b). As expected, the SHG signal is maximal only when focusing near an interface since, as demonstrated before in the literature, SHG vanishes under focusing in the bulk [3]. The process is non-phase-matched because of the Gouy phase shift acquired by the laser beam across the focus. When the collection NA is reduced, less signal is collected (obviously), but it is important to note that the shape of the signal profile is also changing. When the collection NA is larger or equal to 0.55, it is difficult to determine from the SHG signal profile the position of the focal plane relative to the air-crystal interface. However, when the collection NA is smaller than a critical value of 0.3, the SHG profile curves become asymmetric. The signal drops more drastically when the focal plane is in the crystal than when it is in the air. This asymmetry in the SHG signal relative to the air-$\chi^{(2)}$ interface can be used to determine if the focal plane is in or out the noncentrosymmetric medium.

This indicates that, when focusing near the interface in the air, the SHG must be mostly forward emitted because the shape of the profile is maintained when reducing the collection NA. Also, when focusing in the crystal, the SHG must be emitted at a higher angle from the optical axis because the signal drops more rapidly and the shape of the profile changes when reducing the collection NA. As discussed previously in the literature, the radiation pattern depends of the distribution of $\chi^{(2)}$ scatterers within the focal volume [28]. It is also important to note that two different arrangements of $\chi^{(2)}$ scatterers within the focal volume, although generating the same SHG signal, can be differentiated using the radiation pattern.

To confirm this change in the radiation pattern, the last experiment was repeated, but the PMT used to measure the SHG signal was replaced by a CCD camera taking images of the radiation pattern. The iris was fully opened to let all the SHG light reach the camera. It is critical for this part of the experiment that the SHG beam stay collimated to get accurate results when taking images with the CCD camera. Divergence affects the scale of the image taken and is a source of error. With this setup, the radial distribution of the intensity in the collimated beam of SHG leaving the collection objective corresponds to the angular intensity distribution of the signal generated by the sample (also called, the radiation pattern). The images taken (Fig. 4(c-h)) while focusing at different position near the interface (Fig. 4(i)) clearly confirm that the radiation pattern is a uniform cross section of the beam when the focal plane is in the air (Fig. 4(g-h)) while, when it is in the bulk of the crystal (Fig. 4(c-e)), it is ring shaped with intensity concentrated on the edges and ripples in the middle. Note that the ripples present in the images are also found in the SHG profiles with reduced collection NA. The radial intensity distributions for the images of Fig. 4 (c-h) are also presented in Fig. 4 (j).

This model in crystalline quartz confirms that reducing the collection NA is a simple approach to detect changes in the radiation pattern. Since the radiation pattern depends on the distribution of the $\chi^{(2)}$ scatterers in the focal volume, the observation of new features in the forward SHG fascia images (Fig. 3) while reducing the collection NA is a clear experimental indication that the distribution of $\chi^{(2)}$ scatterers is heterogeneous at the sub-micron scale.

3.4 Piezoresponse force microscopy imaging of fascia

In PFM, one detects a material mechanical displacement (expansion/contraction or a lateral displacement) induced by a low frequency electric field primarily acting on the ions. In SHG, 2ω light is generated because electrons are displaced within the noncentrosymmetric ionic potentials by the high frequency electric field component of the laser radiation. PFM provides high spatial resolution (sub-10 nm) and allows imaging structures lacking a center of inversion (noncentrosymmetric - piezoelectric). This resolution is superior by almost two orders of magnitude to that provided by the nonlinear optical microscope.

Therefore, to investigate the structural origin of imaging contrast observed in the SHG experiments, we analyzed similar samples using PFM. Figure 5 shows a typical PFM experiment: a) topography obtained by AFM, b) zoom of the framed region in a) and c) Piezoresponse Force Microscopy – PFM of the region imaged in b). As shown in our previous work [41], fascia is composed of two distinct layers, the top one (on the muscle side) consisting of quasi-randomly-oriented fibers and fiber bundles and a second one, composed of parallel, separate collagen fiber bundles. In the experiments presented here, the top layer of fascia has been removed, in order to eliminate the scatterers with random orientation. Each fiber bundle in the bottom layer of fascia is 2-10 microns wide (as seen in the topographic image in Fig. 5(a), and we estimate that one single collagen fibril is around 30 nm in diameter). The 67 nm periodicity of the banding pattern characterizing collagen type I fibrils is clearly visible in the higher magnification image in Fig. 5(b) [31–33].

The PFM image (Fig. 5(c)) reveals that the piezoelectric response in fascia has either a positive or negative value (white or a dark contrast), constant over large distances along the collagen fibrils. The detected piezoresponse being in-plane, we deduced that the piezoelectric tensor of the fibrils exhibits an axial symmetry, with the axis parallel to the fibril length. Within fascia, the fibrils are organized in "nano-domains", groups of adjacent fibrils having the same polar orientation. From the width of the domains, we deduce that in average 2-3

fibrils form such a group. Since the PFM technique is sensitive mainly to the surface (few nanometers to few tens of nanometers, depending on the contact mechanics), we extrapolate that the nano-domains have a similar size in the depth of fascia.
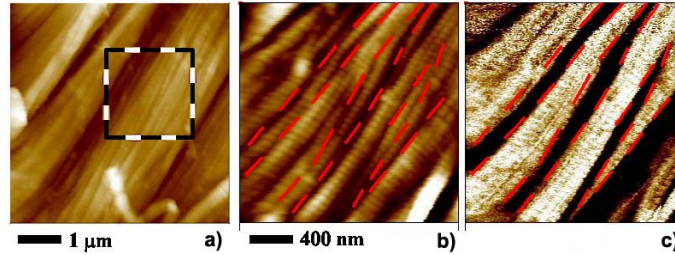

Fig. 5. Piezoresponse force microscopy experiment on fascia. a) sample topography, 5μm scan, (b) topography, zoom of (a), and (c) piezoresponse image [of the same area as in (b)] showing the orientation of the piezoelectric tensor. The piezoelectric response in fascia has either a positive or negative value (white or a dark contrast).

To further confirm the structural origin of noncentrosymmetricity in fascia, we analyzed the piezoelectric response of one single isolated fibril (Fig. 6, see next page) in order to clarify the imaging contrast observed in the PFM image of Fig. 5(c). For this purpose, we recorded several PFM images of the same location at different orientations between the cantilever of the collagen fibril, by rotating the sample under the probing tip. In Fig. 6, we show the dependence of the PFM signal on the angle between cantilever and the fibril axis. The PFM signal could be fit with a cosine function, implying that the piezoelectric response is primarily a shear displacement along the fibril axis. The insets of Fig. 6 show two of the images used to calculate the points of the graph. The results presented in this last figure are showing that isolated collagen fibrils are noncentrosymmetric (piezoelectric) and that the sign of the second order nonlinear optical susceptibility is maintained along the fibrillar axis over several microns. Additionally, a careful analysis of the signal strength generated by isolated fibrils, as well as comparison with results on collagen from bovine [42] have shown that the signal is uniform across the fibril diameter, suggesting that the the whole volume of the fibril is piezoelectric and not only the surface. Indeed, as Kholkin et al. observed in peptide nanotubes, the PFM signal is maximum at the edge (corresponding to the tube wall) and
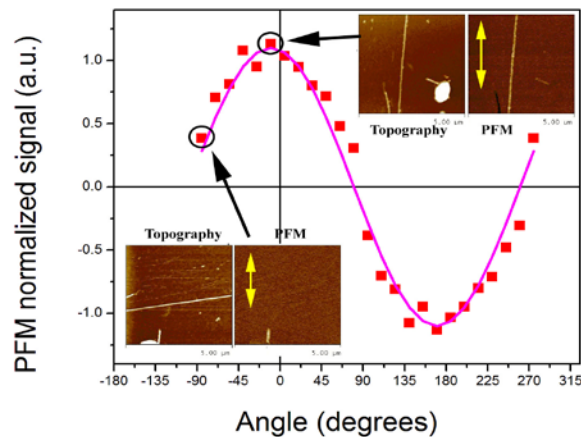

Fig. 6. The dependence of the PFM signal (in-plane measurements) on the angle between the cantilever and the collagen fibril axis, averaged over a 5μm of fibril length. The single collagen fibril was rotated in steps of 15 degrees. The insets illustrate two of the image sets (each composed of topography at left and PFM image at right, 5μm scans) used to construct the graph. The yellow arrows in the PFM images illustrate the detection direction.

clearly decreases at the center (corresponding to on the crest of the tube) when the tube wall is thin [43]. A non-homogeneous distribution (such as "core-shell") of piezoelectric material within the fibril would thus imply a weaker PFM response of the thin piezoelectric shell in the central region. Therefore, the high-resolution PFM results support one of the models proposed by Strupler and Schanne-Klein to simulate SHG from tissues rich in collagen type I proteins, where the $\chi^{(2)}$ scatterers are distributed uniformly within the volume of the fibrils represented as cylinders, and the phase of $\chi^{(2)}$ is allowed to flip by 180 degrees from one fibril to another [37].

4. Conclusion

In this paper, we used second harmonic generation and piezoresponse force microscopy techniques to image noncentrosymmetric structures in fascia. The measurements performed with SHG microscopy reveal that the distribution of $\chi^{(2)}$ scatterers is heterogeneous on a spatial scale inferior to the resolution provided by the nonlinear optical microscope (sub-micron). Comparing forward and backward images indicates that the continuous patterns observed in the direction of laser propagation are not fibers but regions where the phase matching condition is better satisfied. In the backward direction, the SHG signal is nearly uniform across the collagen sheets of fascia revealing that noncentrosymmetric structures are present everywhere within the spatial resolution provided by the nonlinear optical microscope. Furthermore, the large modulations observed in the forward SHG images suggest that the nanoscale architecture of $\chi^{(2)}$ scatterers changes rapidly in the transverse direction to the fibrillar axis. Measurements of the forward signal as a function of the numerical aperture of collection lead to the same conclusion but along the direction of laser propagation.

Using piezoresponse force microscopy, a scanning probe technique also sensitive to the presence of noncentrosymmetric structures and providing sub-10 nm spatial resolution, we demonstrated that an individual collagen fibril has a noncentrosymmetric structural organization, with an anisotropic axis maintained along the fibrillar axis. Fibrils are found to be organized into nano-domains where the anisotropic axis is uniformly directed along the fibrillar axis. Across the collagen sheets of fascia, in the direction transverse to the fibrillar axis, the phase of the second order nonlinear susceptibility is changing by 180 degrees between adjacent nano-domains. We extrapolate that they have a similar size in the depth of fascia. The experimental results presented in this paper confirm the essence of one model used by Strupler and Schanne-Klein to simulate SHG from tendon, namely a uniform distribution of scatterers throughout the whole fibril volume with random 180° polarization flips [30], a tissue rich in collagen type I proteins like fascia. The complex nanoscale architecture of $\chi^{(2)}$ scatterers governs the phase matching condition and allows forward and backward SHG in the bulk of collagen tissues as opposed to SHG in the bulk of homogenous crystal such as quartz. An analogy with periodically poled crystals used for efficient SHG conversion can be drawn, but in the case of tissues rich in collagen type I proteins, the periodicity is not well defined and changes across the collagen sheets. Henceforth, describing fascia as a nanometric randomly poled crystal would be more accurate.